DOI: 10.30511/pcdp.2024.719229 - ISSN: 3060-8376 - Vol 1(1), 2024

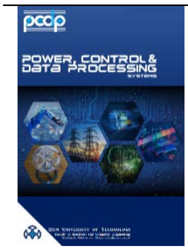

POWER, CONTROL AND
DATA PROCESSING SYSTEMS
Available Online at: https://pcdp.qut.ac.ir/

Adaptive Beamforming for Improved Ultrasonic Imaging in Noisy Environments

ARTICLE INFO

Article Type
Original Research

Authors
Mehdi Bekrani[1]

[1] Department of electrical and computer engineering, Qom University of Technology, Qom, Iran,
bekrani@qut.ac.ir

**** Correspondence***
Address: Department of electrical and computer engineering, Qom University of Technology, Khodakaram Boulevard, Qom, Iran. Postal Code:71551313.
Phone: -
Fax: -
bekrani@qut.ac.ir

Article History
Received: November 09, 2024
Accepted: November 23, 2024
ePublished: December 01, 2024

ABSTRACT

In this paper, we introduce a novel Delay-Weight-Sum (DWS) beamforming technique for defect detection in non-destructive testing (NDT). This method offers improved accuracy over traditional Total Focusing Method (TFM) and its weighted variants. The proposed technique enhances defect detection and imaging quality through an advanced DWS beamforming approach based on a minimum variance method. The minimum variance approach utilizes the Newton-Schulz iterative method for efficient matrix inverse approximation. Additionally, a new non-linear weighting mechanism, based on a sigmoid function, is introduced to refine the matrix inverse approximation for DWS beamforming. This mechanism dynamically adjusts the weighting to enhance reflective points while reducing background noise. Comparative analyses demonstrate the superior imaging resolution and reduced background noise achieved by the proposed method compared to existing TFM-based techniques. Despite its computational demands, simulation results show that the method significantly improves ultrasonic image quality and contrast, holding promise for advancements in ultrasonic NDT, especially in heterogeneous and noisy environments.

Keywords: Ultrasonic imaging; Ultrasonic phased array; Beamforming; Total focusing method; Minimum Variance.

1 Introduction

Ultrasonic phased arrays have undergone substantial advancements in non-destructive testing (NDT), significantly improving defect detection capabilities in test specimens. These advancements are largely attributed to their superior performance compared to conventional single-element transmitter/receiver systems. A key advantage of phased arrays is their ability to generate real-time, integrated images of the test specimen. In scanning methods for defect detection, data is acquired through the phased array elements, which is subsequently processed to produce an ultrasonic image [1, 2].

Common scanning techniques for phased arrays include planar, sectorial, and focused scanning methods [3, 4, 5]. Among these, methods based on Delay-and-Sum (DAS) beamforming, such as the Total Focusing Method (TFM) and the Synthetic Aperture Focusing Technique (SAFT), are commonly employed to construct ultrasonic images [6, 7, 8].

The TFM has become a cornerstone in the field of ultrasonic NDT, offering high-resolution imaging capabilities essential for inspecting a variety of complex materials, including composites, titanium, and rubber [9, 10, 11]. The ability of TFM to process large amounts of data from full matrix capture (FMC) allows for precise defect detection and localization, but its application is challenged by the high level of backscattering in complex materials [12]. This scattering can obscure defect signals, making defect imaging and localization difficult.

To address these challenges, researchers have developed new algorithms and techniques to enhance TFM's performance. One such approach involves combining Golay code excitation with linear frequency modulation and an improved single-excitation method. This method not only improves the signal-to-noise ratio (SNR) but also enhances axial and depth resolution, resulting in superior imaging performance [12, 13]. Moreover, the introduction of compressive sensing techniques reduces data requirements significantly, which is crucial for applications with real-time requirements [14]. These methods allow efficient signal recovery even below Nyquist sampling rates, significantly accelerating image formation and reducing computational demands.

Optimizing TFM algorithms has also been a focus, with improvements such as the phase coherence imaging based on the vector coherence factor. This approach uses a lightweight data acquisition process that combines single-bit digitization and phase retrieval [15]. Studies on material anisotropy further demonstrate the potential of optimized TFM algorithms. For example, an improved sound ray tracing method based on the Dijkstra shortest path algorithm for ultrasonic wave propagation analysis was shown to enhance defect detection in special multilayer plates [16]. Additionally, combining coded excitation with single-bit data capture has been shown to enhance TFM imaging performance. The coded excitation pulse compression process enables high SNR images for phase coherence imaging and TFM, with minimal degradation in imaging quality despite reduced data resolution [17]. To further improve efficiency, the discrete slime mold algorithm (DSMA) was proposed for optimizing sparse arrays in TFM. Unlike traditional optimization methods, DSMA uses real-number encoding, avoiding local optima and reducing computational intensity. This method significantly reduces imaging time while maintaining high-quality imaging and surpassing conventional methods in array performance indicator (API) and SNR [18].

Recent advancements in adaptive beamforming techniques have significantly contributed to NDT and ultrasonic imaging applications. Among these methods, the Delay-Weight-Sum (DWS) beamforming approach has emerged as a powerful tool for addressing noise and interference challenges in complex environments [19, 20, 21]. By employing weights derived through the minimum variance (MV) method, DWS effectively mitigates false echoes caused by randomly distributed scatterers, which are commonly encountered in heterogeneous materials such as stainless steel, carbon composites, and concrete [22]. This robust interference suppression capability has further extended its utility to ultrasonic medical imaging applications [23, 24].

The MV beamformer improves ultrasound image resolution and contrast by adaptively calculating weights based on the spatial covariance matrix [25, 26, 24]. Recent innovations, such as the eigenspace-based MV beamformer, further enhance noise suppression by projecting weight vectors into the signal subspace [27]. However, its practical deployment faces significant challenges due to the computational demands of estimating the covariance matrix and leads to a higher computational costs compared to traditional DAS beamforming [28, 29]. Efforts to address these limitations include the use of singular value decomposition (SVD) to improve contrast [27], although this method often lacks a clear criterion for discarding small eigenvalues, potentially compromising speckle texture preservation [30]. Alternative strategies for reducing computational complexity, such as leveraging principal component analysis (PCA) [31] and Legendre polynomials [32], have been explored, along with independent component analysis (ICA) for estimating apodization weights [33].

The aim of this paper is to introduce a DWS beamforming technique to achieve improved defect detection in test specimens. Novelties of the proposed method are as follows:

1. Dynamic Beamforming Weight Adjustment: Introduction of a novel variable MV beamforming technique, dynamically transitioning between MV and DAS beamforming. This enhances peak sensitivity and suppresses noise.

2. Adaptive Weighting via Sigmoid Function: Utilization of a sigmoid function to improve sensi-

tivity to reflective points and enabling effective noise suppression.

3. Efficient Iterative Approximation: Application of the Newton-Schulz method for iterative approximation of the inverse of the input correlation matrix.
4. Flexibility for Diverse Imaging Scenarios: Adjustable parameters, make the method robust and adaptable to a wide range of ultrasonic imaging applications.

The paper is structured as follows: Section 2 provides an overview of TFM beamforming method and extensions of TFM, which incorporate DWS beamforming. Section 3 introduces the proposed DWS method, while Section 4 outlines the evaluation metrics used in this study. Section 5 presents the simulation results, and finally, Section 6 concludes with a discussion of findings and a summary of the results.

2 TFM-based Beamforming Methods

Here, we describe some well-known beamforming methods which are based on TFM.

2.1 TFM

The TFM is a post-processing imaging technique widely utilized in ultrasonic NDT. It relies on the FMC, where data is acquired using an array of transducers, and all possible combinations of transmitters and receivers are processed to produce a high-resolution image of the test specimen [4, 6, 34, 35].

The image intensity at a target point t with coordinates (x, z)—where z denotes the depth and x indicates the lateral position—is computed as follows:

$$q(t) = \sum_{i,j} S_{i,j}(t - \delta_{i,j}), \tag{1}$$

where $S_{i,j}(t)$ represents the signal transmitted by transducer element i and received by element j after being reflected from flaws or voids within the test specimen. The term $\delta_{i,j}$ corresponds to the time taken by the wave to travel from element i to the target point t and back to element j.

By leveraging the complete dataset for each target point, TFM maximizes the use of available information, resulting in highly detailed and accurate imaging [4].

2.2 Weighted TFM (WTFM)

The WTFM method, as a DWS Beamforming, is developed to enhance defect detection in ultrasonic imaging [19]. This method integrates spatial filtering with weighted beamforming, using statistical analysis of data samples based on the MV theory to calculate the weights.

Compared to the standard TFM method, WTFM achieves significant noise reduction and improves image resolution. Assuming the probe consists of N elements, the time-delayed output vector can be expressed as:

$$\mathbf{y}(t) = [y_1(t), y_2(t), \dots, y_N(t)]^T, \tag{2}$$

where $y_i(t)$ represents the delayed output signal from the ith element. The beamformer output is then computed as:

$$z(t) = \mathbf{w}^T \mathbf{y}(t), \tag{3}$$

where $\mathbf{w}$ is the weight vector.

To determine the optimal weights, the optimization problem is formulated as:

$$\mathbf{w}_{\text{opt}} = \frac{\mathbf{R}^{-1}(t)\mathbf{a}}{\mathbf{a}^T \mathbf{R}^{-1}(t)\mathbf{a}}, \tag{4}$$

where $\mathbf{a}$ is a vector of ones, defined as:

$$\mathbf{a} = [1, 1, \dots, 1]^T, \tag{5}$$

and $\mathbf{R}(t)$ represents the autocorrelation matrix of the element output samples, given by:

$$\mathbf{R}(t) = \mathbb{E}[\mathbf{y}(t)\mathbf{y}^T(t)], \tag{6}$$

where $\mathbb{E}[\cdot]$ denotes the expectation operator.

By incorporating this weighting approach, WTFM offers improved defect detection performance, leveraging the spatial coherence of the received signals while suppressing noise and interference.

In practical applications, to accelerate algorithm execution, instantaneous vector values can be used instead of averaging for autocorrelation calculation. As a result, the instantaneous autocorrelation matrix is approximated as:

$$\mathbf{R}(t) \approx \mathbf{y}(t)\mathbf{y}^T(t). \tag{7}$$

For matrix inversion in WTFM, we use the Gauss-Jordan method, which provides a systematic procedure for inverting square matrices without explicitly calculating determinants. Instead, it employs step-by-step row operations, as described in [36]. While this method is straightforward and efficient for small matrices, it becomes computationally intensive for larger ones due to the high number of arithmetic operations required. Additionally, the method can suffer from numerical instability, especially when applied to ill-conditioned matrices in floating-point arithmetic [37].

To mitigate these numerical instabilities and ensure the invertibility of the matrix $\mathbf{R}(t)$, the Regularized Weighted Total Focusing Method (RWTFM) incorporates regularization, expressed as:

$$\mathbf{R}_\eta(t) = \mathbf{R}(t) + \eta \mathbf{I}, \tag{8}$$

where η is a small positive constant, and $\mathbf{I}$ is the identity matrix.

The RWTFM method demonstrates reduced defect detection capability compared to WTFM; however, it is more robust to noise present in A-scan signals, effectively suppressing background noise in the resulting ultrasonic image. While both WTFM and RWTFM methods exhibit superior imaging performance compared to TFM, they involve higher computational complexity due to the matrix inversion operation.

2.3 DWTFM Method

For practical applications, limitations of WTFM and RWTFM make them less favorable compared to more efficient matrix inverse computation techniques.

In the DWTFM method, to enhance the execution speed of the RWTFM approach, instead of using the full autocorrelation matrix, only its diagonal elements are considered, forming a diagonal matrix [38]. Consequently, inverting this matrix only requires inverting its diagonal elements. In this case, the elements of the vector $\mathbf{W}_{\text{opt}}$ transform into

$$\mathbf{w}_{\text{opt}} = \frac{\mathbf{\Lambda}(t)\mathbf{a}}{\mathbf{a}^H \mathbf{\Lambda}(t)\mathbf{a}}, \tag{9}$$

where $\mathbf{\Lambda}(t) = \frac{1}{\mathrm{diag}[\mathbf{R}_\eta(t)]}$. As a result, we obtain

$$w_{\text{opt},i} = \frac{1}{(x_i^2 + \eta)\sum\limits_j \frac{1}{x_j^2+\eta}} \tag{10}$$

where x_i represents the output of ith element at time t. Thus, the computational burden for calculating the optimal weights is significantly reduced compared to the WTFM and RWTFM methods.

This method, despite its simplicity, cannot effectively utilize the information in the received signals to suppress noise and detect defects. Therefore, it has limited performance in enhancing the quality of ultrasonic images [39].

2.4 SWTFM Method

The Newton-Schulz method is an efficient algorithm for approximating the inverse of a matrix [40]. It is widely applied in scenarios where fast and approximate matrix inversions are essential, such as in machine learning, control systems, and numerical simulations [41, 42].

In the Newton-Schulz-based WTFM (SWTFM), the computation of weights, as defined in Eq. 4, is performed using an approximation of the matrix inverse through the Newton-Schulz method. This approach reduces computational complexity compared to direct matrix inversion while maintaining adequate accuracy.

The Newton-Schulz method is an iterative algorithm particularly effective for well-conditioned matrices when an initial guess for the inverse is available. The iterative update formula for approximating the inverse of a square matrix $\mathbf{R}(t)$ is given by:

$$\Phi_{n+1,t} = 2\Phi_{n,t} - \Phi_{n,t}\mathbf{R}(t)\Phi_{n,t}, \quad n = 0, 1, 2, \ldots \tag{11}$$

where $\Phi_{n,t}$ represents the nth approximation of $\mathbf{R}^{-1}(t)$.

The SWTFM method begins by initializing the approximation with an initial guess $\Phi_{0,t}$, typically chosen as:

$$\Phi_{0,t} = \gamma\mathbf{I}, \quad \text{where } \gamma = \frac{1}{\|\mathbf{R}(t)\|}.$$

Here, $\|\mathbf{R}(t)\|$ represents an appropriate matrix norm, such as the Frobenius norm or spectral norm. The choice of γ ensures that the iterations start close to the desired inverse.

The iterations continue until the relative error satisfies the condition:

$$\|\mathbf{I} - \mathbf{R}(t)\Phi_{n,t}\| < \epsilon, \tag{12}$$

where ϵ is a user-defined tolerance specifying the desired accuracy.

The convergence of the Newton-Schulz method is quadratic, meaning the error reduces significantly with each iteration, provided the spectral radius of $\mathbf{I} - \gamma\mathbf{R}(t)$ satisfies:

$$\rho(\mathbf{I} - \gamma\mathbf{R}(t)) < 1.$$

This ensures rapid convergence of the sequence $\{\Phi_{n,t}\}$ to $\mathbf{R}^{-1}(t)$, given a suitable initial guess.

The Newton-Schulz method offers several advantages. Its quadratic convergence allows for rapid refinement of the approximation, and the reliance on matrix-matrix operations makes it highly parallelizable, which is advantageous for large-scale computations. However, the method has some limitations. It requires the matrix $\mathbf{R}(t)$ to be nonsingular and well-conditioned for effective convergence. Additionally, the choice of the initial guess $\Phi_{0,t}$ plays a critical role in determining the speed and success of convergence. By leveraging these properties, the Newton-Schulz method becomes a powerful tool for matrix inverse approximations in computational applications.

The SWTFM method leverages the Newton-Schulz approach to iteratively refine the inverse matrix approximation, enabling efficient weight computation for beamforming. This method strikes a balance between computational efficiency and imaging accuracy, making it a practical choice for scenarios requiring real-time or near-real-time processing.

3 The Proposed Improved SWTFM Method

The goal of our proposed improved SWTFM method is to enhance the accuracy of the original WTFM method, providing better ultrasonic image quality and contrast compared to traditional TFM-based methods. The improved SWTFM method is a two-step technique: in the first step, $q(t)$ is computed using (1). In the second step, a novel variable MV beamforming technique is applied, given by:

$$\mathbf{w}_{\text{opt}} = \frac{\widetilde{\Phi}_t\mathbf{a}}{\mathbf{a}^T\widetilde{\Phi}_t\mathbf{a}}, \tag{13}$$

where $\widetilde{\Phi}_t$ is the approximation of $\widetilde{\mathbf{R}}^{-1}(t)$, defined as:

$$\widetilde{\mathbf{R}}(t) = \alpha(t)\mathbf{R}(t) + (1 - \alpha(t))\mathbf{I}. \tag{14}$$

where $0 \leq \alpha(t) \leq 1$. The approximation $\widetilde{\Phi}_t$ is obtained using the Newton-Schulz method. It can be observed that $\alpha(t)$ regulates $\widetilde{\mathbf{R}}(t)$, causing it to transition between $\mathbf{R}(t)$ and $\mathbf{I}$. Consequently, $\widetilde{\Phi}_t$ varies between $\mathbf{R}^{-1}(t)$ and $\mathbf{I}$. This implies that $\mathbf{w}_{\text{opt}}$ in (13) transitions between the MV beamformer, as defined in (4), and the DAS beamformer, where $\mathbf{w} = \frac{\mathbf{a}}{\mathbf{a}^T\mathbf{a}} = \frac{1}{N}\mathbf{a}$. The output of the beamformer with the latter $\mathbf{w}$ is computed using (3) as

$$z(t) = \frac{1}{N}\mathbf{a}^T\mathbf{y}(t) = \frac{1}{N}\sum_{i=1}^{N} y_i(t), \tag{15}$$

which represents a scaled version of TFM as defined in (1). The goal is to tune $\alpha(t)$ to enhance the peaks of the ultrasonic image, corresponding to reflective points, while suppressing reflections from non-reflective regions. For this purpose, we leverage variations in $q(t)$ to adjust $\alpha(t)$. Consequently, $\alpha(t)$ is designed as a non-linear function of $q(t)$. As $q(t)$ approaches its maximum value, q_M, $\alpha(t)$ approaches zero, and as $q(t)$ approaches its minimum value, q_L, $\alpha(t)$ approaches one. In the extreme case where $\alpha(t) = 1$, we have $\widetilde{\mathbf{R}}(t) = \mathbf{R}(t)$, and the proposed method behaves similarly to SWTFM. Conversely, when $\alpha(t) = 0$, $\widetilde{\mathbf{R}}(t) = \mathbf{I}$, and the proposed method is similar to the TFM approach.

To achieve better sensitivity to the peaks of $q(t)$, which represent reflective points, we utilize a sigmoid function given by:

$$\alpha(t) = \frac{1}{1 + e^{-k(\delta(t) - 0.5)}} \tag{16}$$

where

$$\delta(t) = \frac{q_M - q(t)}{q_M - q_L}. \tag{17}$$

and k is the slope parameter of the function. The larger k is, the steeper the function becomes.

Fig. 1 shows the variation of $\alpha(t)$ with $\delta(t)$ for different values of k. Also Fig. 2 shows the variation of Variation of $\delta(t)$ with $q(t)$.

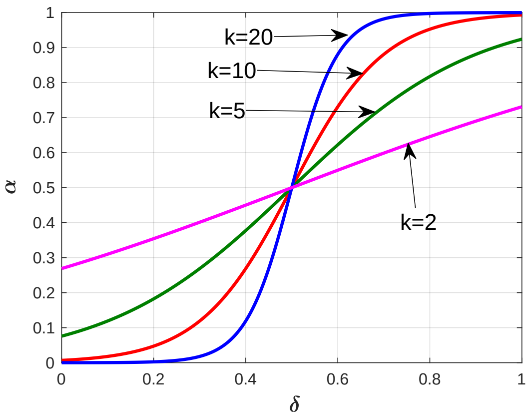

Figure 1: Variation of $\alpha(t)$ with $\delta(t)$ for different values of k.

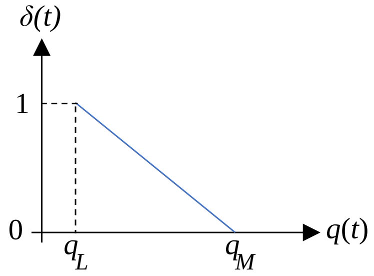

Figure 2: Variation of $\delta(t)$ with $q(t)$.

From Fig. 1, it can be observed that the value of $\alpha(t)$, which is a sigmoid function of $\delta(t)$, increases non-linearly as $\delta(t)$ increases to become near one, or decreases to become near zero. From Fig. 2, it can be observed that $\delta(t)$ is a decaying function of $q(t)$. As a result, $\alpha(t)$ is a non-linear decaying function of $q(t)$. This leads to an enhancement of the peaks (reflecting points) while effectively attenuating the background noise.

Finally, similar to (11), the inverse of $\widetilde{\mathbf{R}}(t)$ can be approximated at each iteration n using the Newton-Schulz method:

$$\widetilde{\Phi}_{n+1,t} = 2\widetilde{\Phi}_{n,t} - \widetilde{\Phi}_{n,t}\widetilde{\mathbf{R}}(t)\widetilde{\Phi}_{n,t}, \quad n = 0, 1, 2, \ldots. \tag{18}$$

The value of $\widetilde{\Phi}_t$ is obtained as $\widetilde{\Phi}_{K,t}$, where K represents the first iteration n for which the following condition is satisfied:

$$\|\mathbf{I} - \widetilde{\mathbf{R}}(t)\widetilde{\Phi}_{n,t}\| < \epsilon. \tag{19}$$

It is notable that the parameter k in the sigmoid function (16) is crucial in determining the sensitivity and convergence rate of the method. It governs the non-linearity of $\alpha(t)$, which directly impacts the weighting of $\mathbf{R}(t)$ and $\mathbf{I}$ in (14). As k increases, the non-linearity becomes more pronounced, resulting in sharper transitions around $\delta(t) = 0.5$. This increases the method's sensitivity to peaks in $q(t)$, thereby highlighting reflective points more distinctly while suppressing background noise. Higher values of k improve resolution by emphasizing reflective points more strongly, but they may also lead to image distortion, such as over-brightness spots, due to abrupt changes in $\alpha(t)$ caused by small fluctuations in $\delta(t)$.

Moreover, a steeper sigmoid function accelerates the transition between the two limits ($\alpha(t) \to 0$ or $\alpha(t) \to 1$). This facilitates faster identification of reflective points and can potentially reduce the number of iterations required by the Newton-Schulz method to achieve convergence.

The iterative approximation of $\widetilde{\Phi}_t$ using the Newton-Schulz method ensures computational efficiency and accuracy. The error in $\widetilde{\Phi}_t$ affects the beamforming weights $\mathbf{w}_{\text{opt}}$, impacting the method's ability to suppress noise and enhance contrast. If $\widetilde{\Phi}_t$ deviates from the true inverse $\widetilde{\mathbf{R}}^{-1}(t)$, the beamforming weights may be suboptimal, potentially leading to reduced contrast and sensitivity in the resulting image. A higher deviation error could lead to increased background noise or diminished peak sensitivity. This trade-off is managed by the iterative approximation process, ensuring (19) is satisfied before the computation of $\mathbf{w}_{\text{opt}}$. By setting an appropriate tolerance ϵ in (19), the trade-off between accuracy and computational cost can be optimized.

Overall, the proposed method achieves improved ultrasonic imaging performance by dynamically adapting to reflective points and effectively reducing background noise. The interplay between the sigmoid function parameter k and the iterative computation of $\widetilde{\Phi}_t$ provides flexibility, enabling the method to be tailored for various imaging scenarios.

The following pseudo-code outlines the steps of the proposed improved SWTFM method to enhance ultrasonic image quality and contrast.

Algorithm 1 Proposed Improved SWTFM Method

```
Input: Signals $S_{i,j}(t)$, target coordinates $(x, z)$, parameters $q_M$, $q_L$, $k$, $\epsilon$
Output: Enhanced Image Intensities $I(x, z)$
Step 1: Initial Coarse Image Computation
for each target point $(x, z)$ do
    Compute $q(t)$ using (1).
end for
Step 2: Adaptive Beamforming
for each target point do
    Compute $\mathbf{R}(t)$ using (7).
    Compute $\delta(t)$ using (17).
    Calculate $\alpha(t)$ using (16).
    Construct $\widetilde{\mathbf{R}}(t)$ using (14).
    Initialize $\Phi_{0,t}$ (initial approximation of $\widetilde{\mathbf{R}}^{-1}(t)$).
    Iterative Newton-Schulz Update:
    for $n = 0, 1, \ldots$ until (19) is satisfied do
        Update $\Phi_{n,t}$ using (18) .
    end for
    Compute optimal beamforming weights $\mathbf{w}_{\text{opt}}$ using (13)
end for
Step 3: Enhanced Image Generation
for each target point $(x, z)$ do
    Combine beamformed signals to produce $I(x, z)$
end for
Return: Enhanced Image $I(x, z)$
```

4 Evaluation Metrics

To perform a quantitative analysis, a brightness intensity function is defined as the maximum intensity value within the depth range of the image $I(x, y)$, computed independently for each x_{ref} as:

$$I_{\max}(x_{\text{ref}}) = \max_{z} \left(I(x_{\text{ref}}, z) \right)$$

where z represents the set of depths within the scanned region. The brightness intensity is then normalized to zero decibels (dB), ensuring that its maximum value corresponds to 0 dB.

For quantifying the results of background noise reduction, the normalized average brightness intensity of non-reflective points within the scanned region is used according to the following equation:

$$\nu = \frac{1}{L} \sum_{x} \sum_{z} I(x, z), \ \forall (x, z) \notin (X, Z) \qquad (20)$$

where (X, Z) denotes the set of coordinates of the defects and L is the total number of scanning points, minus the number of defect members. It is clear that the closer the value of ν to zero, the less background noise, on average, is present. Thus, ν serves as a metric for assessing the overall reduction of background noise. For a better evaluation of changes in ν, this metric is expressed in decibels (dB).

5 Simulation Results

In the simulations, we assume a metallic specimen with a rectangular scan area measuring 50 × 80 mm. A phased array probe with 16 omnidirectional elements, each spaced 5 mm apart, is used. The transmitted signal is a modulated sinusoidal wave with 6 cycles at a central frequency of 6 MHz, sampled at 60 MHz. The sound velocity in the metal is assumed to be 3000 m/s.

White Gaussian noise with a SNR of 0 dB and speckle noise with SNRs of 5 dB and 10 dB are added to the received signals. These noise sources simulate equipment-related transmission and reception noise, as well as reflections from scatterers within the specimen. Following the modeling approach in [4, 19], certain factors—such as coupling, material heterogeneity, wave energy losses, and the generation of secondary waves (e.g., surface, shear, and diffracted waves)—are neglected for simplicity.

To evaluate algorithm performance, four diagonal point defects are placed at coordinates $(50, 15)$, $(40, 20)$, $(30, 25)$, and $(20, 30)$ mm. The experimental setup is depicted in Figure 3. Figure 4 provides an example of an A-scan signal received by the 10th element after transmitting a pulse from the 3rd element, lasting 180 microseconds.

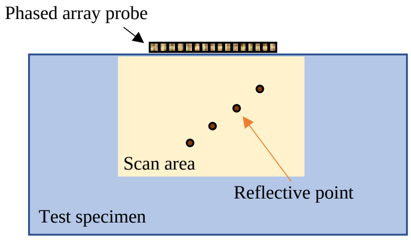

Figure 3: Experimental setup.

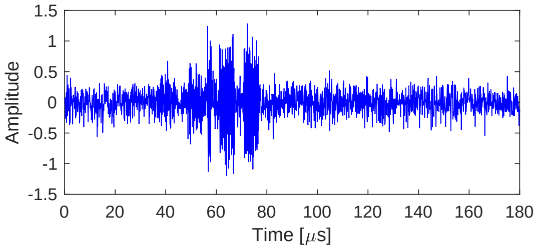

Figure 4: An A-scan signal received by a probe element with $\text{SNR}_{\text{WGN}} = 0$ dB, and $\text{SNR}_{\text{sp}} = 10$ dB.

Based on the wave velocity and the central frequency of the applied signal, the signal's wavelength (indicating the maximum resolution between two reflective points) is calculated as follows:

$$\lambda = \frac{v}{f_c} = 0.5^{\text{mm}}$$

where v is the wave velocity, and f_c is the central frequency of the signal. For the evaluation, we set $\epsilon = 1 \times 10^{-10}$ for SWTFM and limit the maximum number of iterations for approximating the matrix inverse to 10. Additionally, we use $\eta = 0.002$ for DWTFM and $\eta = 0.5$ for RWTFM.

Figure 5 shows the normalized brightness intensity function (in decibels) for the proposed method with different values of k. It is observed that increasing k generally reduces background noise in non-reflective areas. However, noise near reflective points increases, which may lead to a decrease in resolution or contrast in the image. Therefore, selecting the value of k should balance reducing background noise and enhancing the resolution of reflective points.

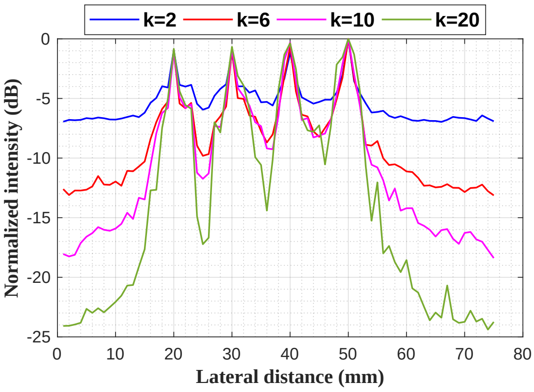

Figure 5: Intensity.

In the subsequent simulations, we assume $k = 6$ for the proposed method. In the first experiment, white noise with $SNR = 0$ dB and speckle noise with $SNR = 10$ dB are added to the signals.

Figure 6 illustrates the brightness intensity function for the RWTFM, TFM, DWTFM, SWTFM, and the proposed method. According to this figure, the aforementioned methods have progressively reduced background noise. Consequently, the reflective points, corresponding to the peaks in the image, are more distinguishable in the proposed method compared to the other methods.

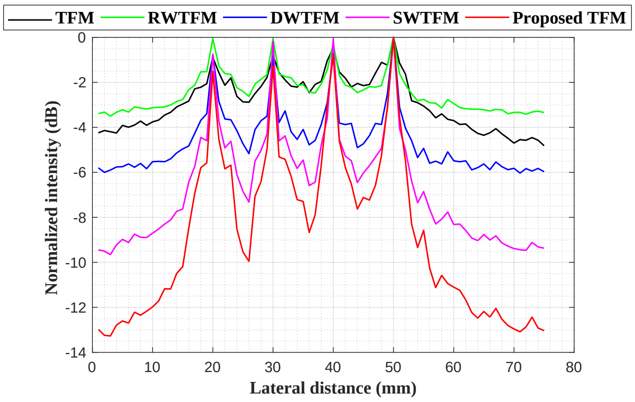

Figure 6: Intensity.

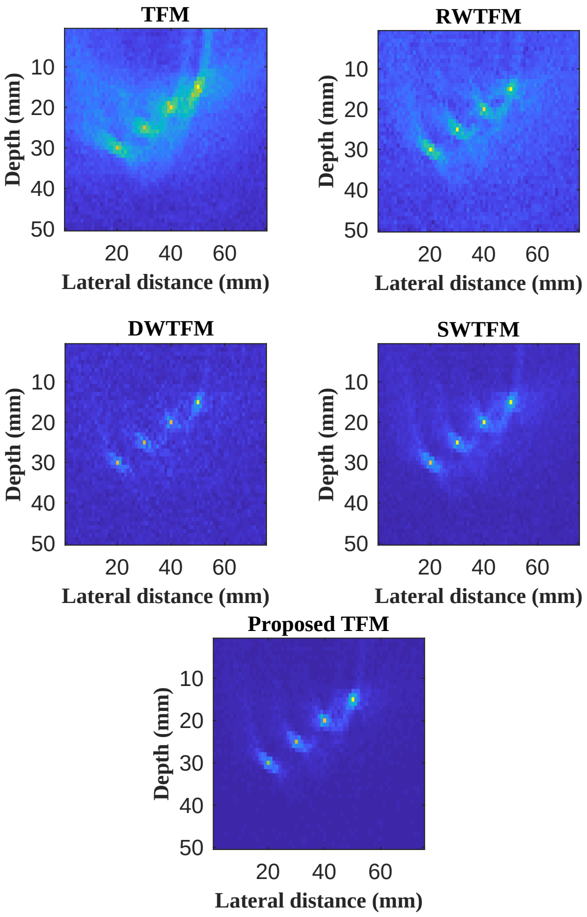

Figure 7: Images obtained from the TFM method, MV method with Gauss-Jordan matrix inversion, MV method with Schur's matrix inversion, and the proposed method.

Figure 7 shows the images obtained by applying the RWTFM, TFM, DWTFM, SWTFM, and the proposed method. As observed, the image produced by the TFM method identifies the locations of all reflective points but suffers from low resolution and cannot accurately determine their positions. Additionally, regions without defects exhibit slight brightness in the image, which may incorrectly be interpreted as additional defects or flaws.

From the figure, it can be seen that the image generated by the RWTFM method partially mitigates the issues inherent in the TFM method. However, significant speckle noise is visible in the image. Moreover, reducing the regularization level η can increase the background noise and decrease the clarity of the image in certain regions with defects. This may result in the potential misinterpretation or omission of one or more defects.

The DWTFM method performs better in this regard, producing images with reduced background noise. Similarly, the SWTFM method further reduces background noise. On the other hand, the image obtained by the proposed method shows that the background noise in defect-free regions is significantly reduced, and the defects are clearly distinguishable.

In the second experiment, white Gaussian noise with $\mathrm{SNR}_{\mathrm{WGN}} = 0$ dB and speckle noise with $\mathrm{SNR}_{\mathrm{sp}} = 5$ dB are introduced. Figure 8 presents a typical A-scan signal from this experiment, captured by the 10th element after transmitting a pulse from the 3rd element, with a duration of 180 microseconds.

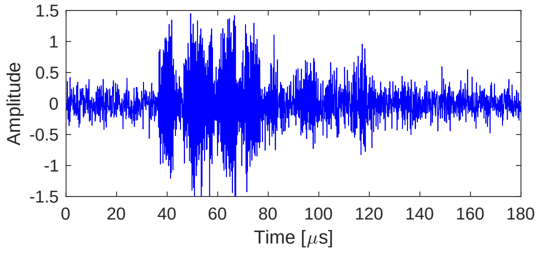

Figure 8: A typical A-scan signal from the second experiment with $\mathrm{SNR}_{\mathrm{WGN}} = 0$ dB, and $\mathrm{SNR}_{\mathrm{sp}} = 5$ dB.

Figure 9 displays the ultrasonic images produced by the methods under investigation. As observed, due to the increased level of speckle noise, the background noise has significantly increased, leading to a higher likelihood of false detection of defects. Additionally, the image of reflective points has become slightly blurred, increasing the probability of missing actual defects.

In the DWTFM method, the background noise is removed much better compared to the TFM and RWTFM methods; however, the image of two reflective points is completely blurred. The SWTFM method performs better than the DWTFM method, but these two issues still persist to some extent. The proposed method, by further reducing the noise level while preserving reflective points, creates a superior image in which all reflective points are clearly distinguishable.

Table 1 quantitatively shows the background noise levels using Eq. 20 for different methods in the first and second experiments. It also shows, in terms of the brightness function, the distance between the peak and the valley for the two neighboring defects located at horizontal distances of 20 and 30 millimeters.

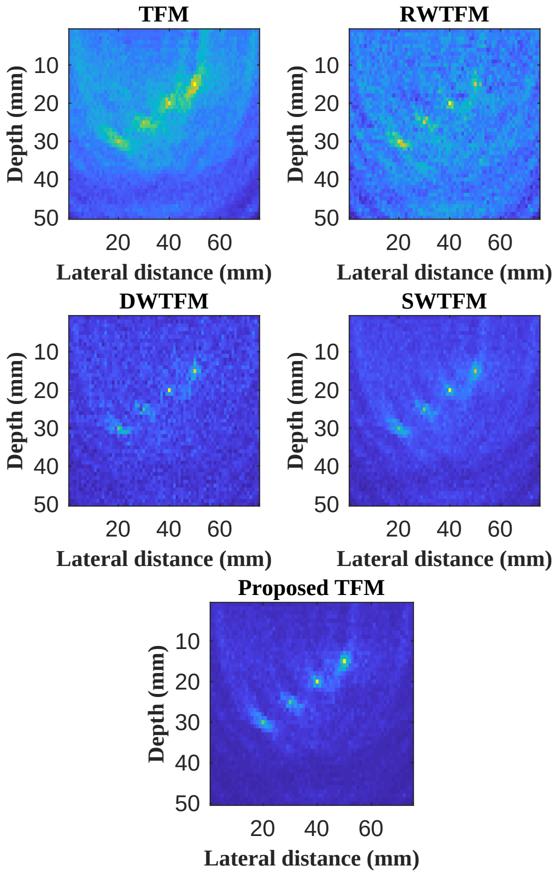

Figure 9: Ultrasonic images obtained from the methods under investigation.

As observed, the peak-to-valley distance Δ in the proposed method is greater than in the other methods, indicating better resolution of adjacent reflective points. Furthermore, the background noise in the proposed method is at least three decibels lower than in the other methods, leading to a clearer image.

Table 1: Background noise and peak-to-trough distance for different methods in the first and second experiments for $SNR_{WGN} = 0$ dB.

	$SNR_{sp} = 5$ dB		$SNR_{sp} = 10$ dB	
Method	e	Δ	e	Δ
TFM	-3.8 dB	1.35 dB	-5.3 dB	1.91 dB
RWTFM	-2.3 dB	1.1 dB	-4.2 dB	2.60 dB
DWTFM	-5.9 dB	3.25 dB	-9.3 dB	5.84 dB
SWTFM	-6.6 dB	3.62 dB	-10.7 dB	6.05 dB
Proposed	-9.9 dB	4.96 dB	-13.7 dB	7.31 dB

Note: e represents the background noise, and Δ denotes the peak-to-trough distance.

6 Conclusion

This paper presents an improved Weighted Total Focusing Method for ultrasonic non-destructive testing (NDT). The method integrates the Newton-Schulz iterative method for efficient matrix inverse approximation and a novel non-linear weighting mechanism based on a sigmoid function for optimized imaging performance. This approach enhances defect detection accuracy and image quality by emphasizing defect-related peaks and suppressing background noise. Comparative analyses show superior imaging contrast and resolution compared to traditional TFM and its weighted variants. Despite its computational complexity, the proposed method improve ultrasonic image quality and contrast, demonstrating significant potential for advancing ultrasonic NDT in heterogeneous and noisy environments.

Disclosure of Potential Conflicts of Interest

The Authors declare that there is no conflict of interest.

References

[1] L. W. Schmerr, “An ultrasonic system,” in Fundamentals of Ultrasonic Nondestructive Evaluation, Springer, pp. 1–13, 2016.

[2] Olympus NDT, “Introduction to phased array ultrasonic technology applications: D Tech Guideline,” Olympus NDT, 2004.

[3] M. Jobst and G. Connolly, “Demonstration of the Application of the Total Focusing Method to the Inspection of Steel Welds,” European Conference on Non-Destructive Testing, pp. 1–11, 2010.

[4] C. Holmes, B. W. Drinkwater, and P. D. Wilcox, “Post-processing of the full matrix of ultrasonic transmit–receive array data for non-destructive evaluation,” NDT & E International, vol. 38, no. 8, pp. 701–711, 2005.

[5] B. W. Drinkwater and P. D. Wilcox, “Ultrasonic arrays for non-destructive evaluation: A review,” NDT & E International, vol. 39, no. 7, pp. 525–541, 2006.

[6] J. Lambert, A. Pédron, G. Gens, F. Bimbard, L. Lacassagne, and E. Lakovleva, “Performance evaluation of total focusing method on GPP and GPU,” Conference on Design and Architectures for Signal and Image Processing (DASIP), pp. 1–8, 2012.

[7] L. Jeune, S. Robert, P. Dumas, A. Membre, and C. Prada, “Adaptive Ultrasonic Imaging with the Total Focusing Method for Inspection of Complex Components Immersed in Water,” AIP Conference Proceedings, vol. 1650, pp. 1037–1046, 2015.

[8] C. Huang and F. Lanza di Scalea, “Application of sparse synthetic aperture focusing techniques to ultrasound imaging in solids using a transducer wedge,” *IEEE Trans. Ultrason., Ferroelectr., Freq. Control*, vol. 71, no. 2, pp. 280–294, Feb. 2024.

[9] X. Yang, E. Verboven, B.-F. Ju, and M. Kersemans, “Comparative study of ultrasonic techniques for reconstructing the multilayer structure of composites," NDT E Int., vol. 121, no. 102460, Jul. 2021.

[10] A. Velichko, E. L. Villaverde, and A. J. Croxford, “Local scattering ultrasound imaging," Sci. Rep., vol. 11, no. 1, p. 993, Jan. 2021.

[11] H. Shi, M. Ebrahimi, P. Zhou, K. Shao, and J. Li, “Ultrasonic and phased-array inspection in titanium-based alloys: A review," Proc. Inst. Mech. Eng., Part E, J. Process Mech. Eng., vol. 237, no. 2, pp. 511–530, Apr. 2023.

[12] Chandler, M. G., Croxford, A. J., and Wilcox, P. D., “A Multivariate Statistical Approach to Wrinkling Detection in Composites," IEEE Transactions on Ultrasonics, Ferroelectrics, and Frequency Control, vol. 71, no. 9, pp. 1141–1151, 2024.

[13] P. Shen, Y. Wu, Z. Luo, Z. Wu, J. Jing, and H. Zhang, “Advanced Orthogonal Frequency and Phase Modulated Waveform for Ultrasonic Phased Array TFM Detection in CFRP Composites," IEEE Transactions on Instrumentation and Measurement, vol. 73, no. 4504410, pp. 1-10, 2024.

[14] L. P. Piedade, G. Painchaud-April, A. Le Duff, and P. Bélanger, “Compressive Sensing Strategy on Sparse Array to Accelerate Ultrasonic TFM Imaging," IEEE Transactions on Ultrasonics, Ferroelectrics, and Frequency Control, vol. 70, no. 6, pp. 538-550, June 2023.

[15] B. Gauthier, G. Painchaud-April, A. Le Duff, and P. Bélanger, “Lightweight and Amplitude-Free Ultrasonic Imaging Using Single-Bit Digitization and Instantaneous Phase Coherence," IEEE Transactions on Ultrasonics, Ferroelectrics, and Frequency Control, vol. 69, no. 5, pp. 1763-1774, May 2022.

[16] Y. -X. Qin, X. -M. Xiong, Y. Chen, and Y. Wang, “Optimization Research on Defect Localization in Ultrasonic Images of Anisotropic and Multilayer CFRP Structures," IEEE Transactions on Instrumentation and Measurement, vol. 73, pp. 1-14, 2024.

[17] E. Nicolson, D. Lines, E. Mohseni, and C. N. MacLeod, “Single-Bit Reception With Coded Excitation for Lightweight Advanced Ultrasonic Imaging Systems," IEEE Transactions on Ultrasonics, Ferroelectrics, and Frequency Control, vol. 71, no. 9, pp. 1120-1131, Sept. 2024.

[18] W. Zhu et al., “Sparse Optimal Design of an Ultrasonic Sensor Array for Fast TFM Based on a Discrete Slime Mold Algorithm," IEEE Sensors Journal, vol. 24, no. 8, pp. 12207-12216, April 2024.

[19] M. Li and G. Hayward, “Ultrasound Nondestructive Evaluation (NDE) Imaging with Transducer

Arrays and Adaptive Processing," Sensors, vol. 12, no. 1, pp. 42–54, 2012.

[20] S. M. Sakhaei, "A decimated minimum variance beamformer applied to ultrasound imaging," Ultrasonics, vol. 59, 2015.

[21] M. Ehsani, M. Bekrani, and S. Garousi, "Robust Beamforming for Ultrasonic Imaging using Wavelet-based Thresholding and Coherence Weighting," *International Journal of Industrial Electronics Control and Optimization*, vol. 7, no. 4, pp. 339–350, 2024.

[22] M. Li and G. Hayward, "Adaptive Array Processing for Enhanced Ultrasonic Non-destructive Evaluation (NDE) and Imaging," Proceedings of the American Institute of Physics (AIP) Conference, vol. 2102, pp. 100007/1–100007/8, May 2019.

[23] S.-L. Pu, H. Guo, H.-W. Xie, C. Chen, P. Zhou, and G.-Q. Zhou, "Minimum Variance Optimizations With Different Covariance Matrices in Plane-Wave Ultrasound Imaging," IEEE Transactions on Instrumentation and Measurement, vol. 73, no. 4509213, pp. 1–13, 2024.

[24] Y. Wang, S. Feng, J. Pan, C. Zheng, H. Peng, and Y. Wang, "Random Matrix Theory-Based Wiener Postfilter Combined With Eigenspace and Spatial Coherence-Based Minimum Variance Beamformer for Coherent Plane-Wave Adaptive Compounding," IEEE Transactions on Instrumentation and Measurement, vol. 73, no. 4503317, pp. 1–17, 2024.

[25] O. M. H. Rindal, J. P. Asen, S. Holm, and A. Austeng, "Understanding contrast improvements from capon beamforming," in *Proc. IEEE Int. Ultrason. Symp.*, pp. 1694–1697, 2014.

[26] K. Diamantis, A. Greenaway, T. Anderson, J. A. Jensen, and V. Sboros, "Experimental performance assessment of the sub-band minimum variance beamformer for ultrasound imaging," Ultrasonics, vol. 79, pp. 87–95, Aug. 2017.

[27] B. M. Asl and A. Mahloojifar, "Eigenspace-based minimum variance beamforming applied to medical ultrasound imaging," *IEEE Trans. Ultrason., Ferroelectr., Freq. Control*, vol. 57, no. 11, pp. 2381–2390, Nov. 2010.

[28] H. Hasegawa and R. Nagaoka, "Improvement of performance of minimum variance beamformer by introducing cross covariance estimate," *J. Med. Ultrason.*, vol. 47, no. 2, pp. 203–210, Apr. 2020.

[29] Z. Zhang, Z. Lei, M. Zhou, H. Hasegawa, and S. Gao, "Complex-valued convolutional gated recurrent neural network for ultrasound beamforming," *IEEE Trans. Neural Netw. Learn. Syst.*, doi: 10.1109/TNNLS.2024.3384314.

[30] S. Goudarzi, A. Basarab, and H. Rivaz, "A unifying approach to inverse problems of ultrasound beamforming and deconvolution," *IEEE Trans. Comput. Imaging*, vol. 9, pp. 197–209, 2023.

[31] K. Kim, S. Park, J. Kim, S. B. Park, and M. Bae, "A fast minimum variance beamforming method using principal component analysis," *IEEE Trans. Ultrason., Ferroelectr., Freq. Control*, vol. 61, no. 6, pp. 930–945, Jun. 2014.

[32] M. Bae, S. B. Park, and S. J. Kwon, "Fast minimum variance beamforming based on Legendre polynomials," *IEEE Trans. Ultrason., Ferroelectr., Freq. Control*, vol. 63, no. 9, pp. 1422–1431, Sep. 2016.

[33] S. Goudarzi, A. Asif, and H. Rivaz, "Plane-wave ultrasound beamforming through independent component analysis," *Comput. Methods Programs Biomed.*, vol. 203, 2021, Art. no. 106036, 2021.

[34] M. Sutcliffe, M. Weston, B. Dutton, and I. Cooper, "Real-Time Full Matrix Capture with Auto-Focusing of Known Geometry through Dual Layered Media," NDT & E International, vol. 51, 2012.

[35] M. J. Simões, F. Santos, and J. B. Santos, "FPGA-Based Control System of an Ultrasonic Phased Array," Journal of Mechanical Engineering, vol. 57, no. 2, 2011.

[36] D. DasGupta, "In-place matrix inversion by modified Gauss-Jordan algorithm," Applied Mathematics, vol. 4, pp. 1392–1396, 2013.

[37] Strang, G., *Introduction to Linear Algebra*, (4th ed.), Wellesley-Cambridge Press, 2009.

[38] M. Bekrani and V. H. Vaghef, "A Novel Method for Imaging and Defect Detection Using Ultrasonic Phased Arrays," Iranian Conference on Mathematical Physics, Qom University of Technology, November 2016.

[39] M. Bekrani and V. H. Vaghef, "Ultrasound Phased Array Imaging with Minimum Variance-Based Beamforming," The 11th Iranian and the 1st International Conference on Machine Vision and Image Processing (MVIP 2020), 2020.

[40] N. J. Higham, "Iterative Refinement for the Solution of Perturbed Linear Systems," SIAM Journal on Matrix Analysis and Applications, vol. 18, no. 4, pp. 1035–1051, 1997.

[41] N. J. Higham, *Accuracy and Stability of Numerical Algorithms*, SIAM Publications, 2002.

[42] G. H. Golub and C. F. Van Loan, *Matrix Computations*, Johns Hopkins University Press, 2013.